PHYSICAL REVIEW APPLIED **18,** 054050 (2022)

Editors' Suggestion

Optimal Design of Three-Dimensional Voxel Printed Multimaterial Lattice Metamaterials via Machine Learning and Evolutionary Algorithm

Le Dong and Dong Wang[*]

Robotics Institute, State Key Laboratory of Mechanical System and Vibration and Meta Robotics Institute, Shanghai Jiao Tong University, Shanghai, 200240, China

(Received 1 July 2022; accepted 3 October 2022; published 16 November 2022)

Mechanical metamaterials could exhibit tremendous design potential through synergistic material distribution and structural design. However, the existing designs mainly focus on the structures and neglect the material distributions. We propose a digital design and optimization method for lattice metamaterials using machine learning and an evolutionary algorithm taking into account both material distributions and structural design. The machine learning model is developed to predict mechanical behaviors accurately, based on the database generated by PYTHON-assisted finite-element simulations with random material and structural parameters. The optimal design is realized by the evolutionary algorithm method, which can quickly find the target mechanical responses in a broad design space. A digital voxel model is established to three-dimensionally print the designed multimaterial lattice metamaterials. The developed framework can be used to match multiple targets, such as reproducing the stress-strain and Poisson's ratio curves of biological tissues simultaneously. Lattice metamaterials with customized lateral profiles are also demonstrated. This work expands the design space of lattice metamaterials and is of great interest in flexible electronics and soft robotics.

DOI: 10.1103/PhysRevApplied.18.054050

I. INTRODUCTION

Mechanical metamaterials are artificial structures composed of an orderly arrangement of microstructures, which may emulate or exceed the versatile behaviors and properties of naturally occurring materials and organisms [1–6]. By structural design, metamaterials exhibit attractive application prospects, such as reversible mechanical diodes [7], lightweight metamaterials for energy absorption [8], intelligent metamaterials for magnetic resonance imaging [9], and four-dimensional (4D) metamaterials with drug-releasing functionality [10]. However, existing designs of metamaterials mainly focus on structural design and neglect the effects of material distribution. In contrast, organisms have ingeniously evolved higher performance materials via synergetic material distribution and complex structures from a relatively limited choice of elements and compounds through long-term evolution and natural selection [11–13]. Examples include the tooth with reliable cyclic mastication functionality [14,15], bone with anticracking property [16], and mantis shrimp appendages with damage avoidance capability [17,18].

One of the main reasons for neglecting multimaterial distribution is the lack of manufacturing methods that can precisely distribute multiple materials. Recent advancements in additive manufacturing have paved the way for manufacturing multimaterial structures [19,20]. A typical example is three-dimensional (3D) voxel printing that comprises jetting multiple base photopolymers followed by ultraviolet (UV) curing to create layer-by-layer multimaterial objects [21,22]. The 3D voxel printing allows users to deposit different materials at each unit volume (voxel) and enables the controllable distribution of materials, in which a matrix is used to define the material identity of each droplet and its placement in 3D space.

The ability to distribute multiple materials precisely increases the mechanical metamaterial's design freedom [23–25], but it simultaneously imposes emerging challenges on design. Specifically, both forward design for predicting mechanical responses and inverse design for optimal material distributions and structures remain challenging due to the enormous design space. To design mechanical metamaterials with predictable mechanical behaviors, several theoretical methods have been proposed, including the nonlinear mechanics model of metamaterials comprising horseshoe microstructures [26], the theoretical framework of network metamaterials with rotatable structural nodes [27], the finite deformation model for polygonal lattice metamaterials [28], and the homogenization method to calculate the nonlinear mechanical response of lattice metamaterials [29–31]. However, these theoretical models only consider the effects of geometries and neglect the material distributions. A few models take into account the macroscale multimaterial distributions, such as the thermally responsive architectures for 2D bimaterial metamaterials [32]. However, it is still unclear how the

---

[*] wang_dong@sjtu.edu.cn

multimaterial distributions on the voxel scale contribute to the properties of mechanical metamaterials. PYTHON-assisted finite-element method (FEM) simulations can be used as a numerical model to study the mechanical behaviors of mechanical metamaterials with multimaterial distributions and have lower trial-and-error costs than experiments. However, the FEM hardly meets the demands of time-intensive iterative calculations and hinders inverse design when combined with optimization approaches [33].

Machine learning (ML) is a form of artificial intelligence that can automatically build the nonlinear mapping relationship between input and output data through learning and testing the database [34–36]. ML algorithms such as artificial natural networks (ANNs) have been gradually developed as predictive models for accurate inverse design owing to their high speed and efficiencies [37–39]. Several aspects of mechanical metamaterials have been explored using ML algorithms, including 4D printed active composite structures [40], cross-chiral metamaterial structures [41], and bioinspired hierarchical composites [42]. Moreover, many optimization algorithms have been developed to fulfill inverse design, including both gradient-based and gradient-free methods. Among them, gradient-free optimization algorithms exhibit better capabilities of searching for the global optimum and depend less on the initial value than gradient-based topology optimization. For instance, gradient-free optimization algorithms such as evolutionary algorithms (EA) have been applied to solve complex nonlinear optimization problems in metamaterials [43–45]. Therefore, combining ML and EA can provide a promising way to design mechanical metamaterials with tunable material distributions and structures.

In this work, we propose a digital design and optimization method for lattice metamaterials to simultaneously realize multitarget mechanical behaviors using material distribution and structural designs. The design workflow is shown in Fig. 1. First, the digital voxel model is established by tuning the material distributions and geometric design. Next, the ANN-based ML model is used to accurately predict the mechanical behaviors via training the databases constructed by PYTHON-assisted FEM simulations. The optimal design is then realized by integrating the ML model with the EA method, which can quickly find the target mechanical responses in a broad design space. The developed framework can be used to reproduce the strain-stress and strain-Poisson's ratio curves of biological tissues simultaneously. Lattice metamaterials with customized lateral profiles are also demonstrated. Results show that the design space of lattice metamaterials is significantly improved by incorporating the material distributions. This work paves the way for designing the mechanical responses of lattice metamaterials using both material distribution and structural design with potential applications in flexible electronics and soft robotics.

II. DIGITAL DESIGN AND MANUFACTURING WORKFLOW

Figure 1 depicts the digital design process for multimaterial lattice metamaterials. The multimaterial lattice metamaterials are constructed from periodic triangular units with three microstructures. The microstructures are generated by a curvature function $R(\alpha) = \alpha^n$ ($n \in [1\ 3]$ and $\alpha \in [0\ \alpha_{\text{end}}]$) that represents the relationship between the instantaneous radius of curvature (the radius of the osculating circle at the point) R and the slope angle α. The upper left half of the microstructure is first generated using the curvature equation. The bottom right half is the antisymmetric shape of the upper left half with respect to the origin (Fig. S1 within the Supplemental Material [46]). $R(\alpha) = \alpha^n$ is chosen due to the following advantages: (1) R monotonically increases from 0 with α, leading to chirality in the microstructure and improving the stretchability effectively; (2) the shape of the microstructure changes by varying n, leading to continuously and widely tunable J-shaped stress-strain curves; and (3) optimization can be performed by searching for the optimal n.

The coordinates x and y of the microstructure can be obtained from

$$\begin{pmatrix} x(\alpha) \\ y(\alpha) \end{pmatrix} = \int_{o}^{\alpha} R(\alpha) \begin{pmatrix} \cos\ \alpha \\ \sin\ \alpha \end{pmatrix} d\alpha. \quad (1)$$

α_{end} is given by solving the displacement conditions

$$y(\alpha_{\text{end}}) = 0. \quad (2)$$

All microstructures are scaled to $L_M = 10\sqrt{2}$ mm, where L_M is the distance between the two ends of the microstructures. The in-plane thickness $w = 0.4$ mm and out-of-plane thickness $d = 3$ mm.

The material distributions are realized by mixing hard and soft materials at specific volume fractions on a voxel scale. Figure 2 shows the voxel printing procedures for the lattice metamaterials. A commercial material jetting 3D printer (Stratasys J750) is used to fabricate the multimaterial lattice metamaterials. The 3D printing process starts by slicing the stereolithography (STL) file layer by layer, followed by forming the voxel matrix. A MATLAB script is used to generate the voxel matrix by assigning soft and hard materials in each voxel according to the desired modulus. The dimension of each voxel is 600 × 300 × 940 DPI. Agilus (Stratasys, MN, USA) and Veroblue (Stratasys, MN, USA) are chosen as the soft and hard materials. The Young's moduli of Agilus and Veroblue are 0.5 MPa and 1.5 GPa, respectively. The Poisson's ratios are $\nu = 0.3$. The parameter E is the Young's modulus of the material used for manufacturing the metamaterials. By varying the volume fractions of the two materials, Young's modulus (E) can be changed by over 3 orders of magnitude (from 0.5 MPa to 1.5 GPa). The relationship between Young's

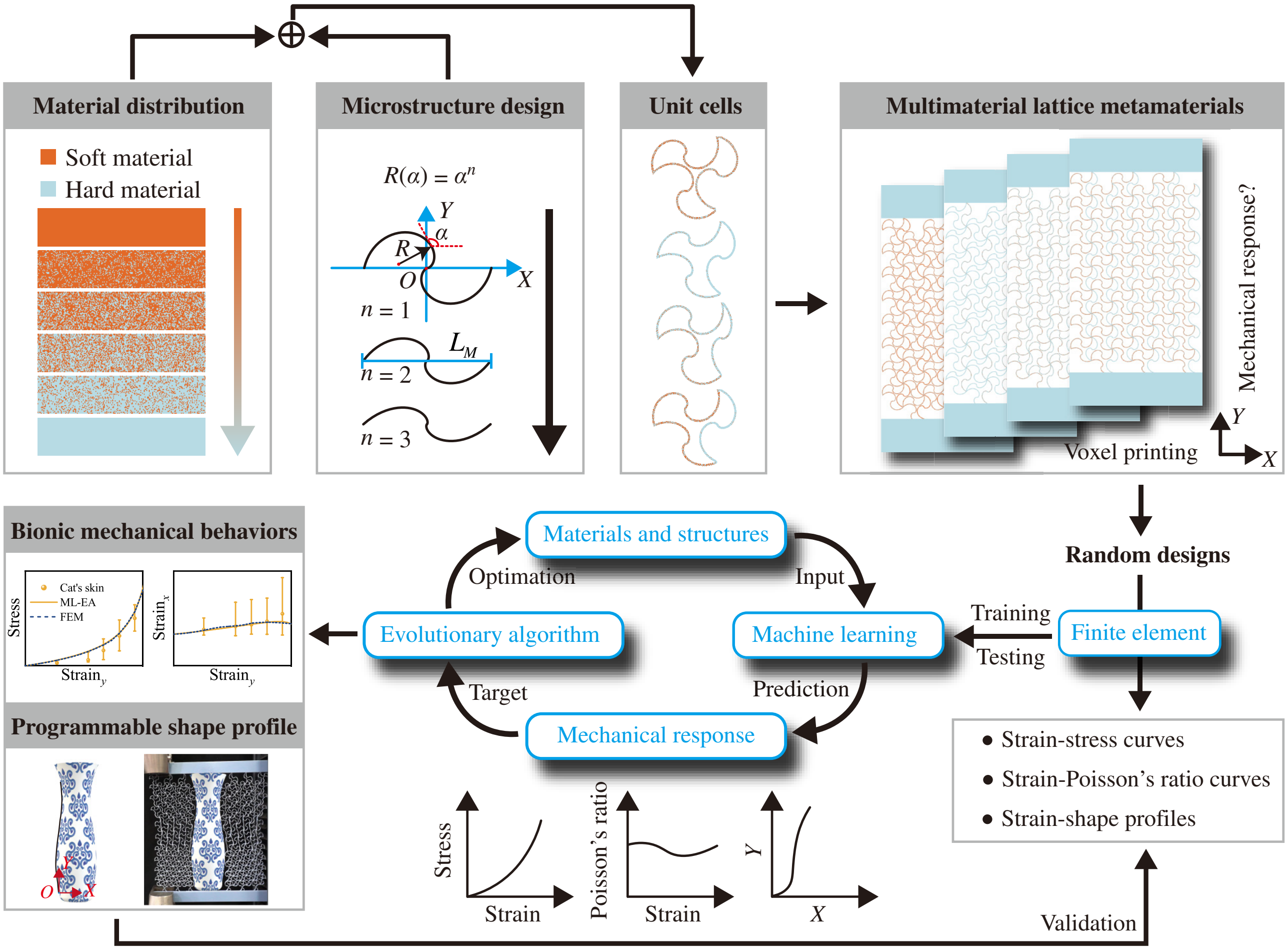

FIG. 1. The digital design and optimization of multimaterial lattice metamaterials. The main workflow includes generating the digital voxel models via tuning the material distributions and parametric microstructures, database formation by FEM simulation, training of the ML model mapping the material and structural parameters to the mechanical responses, ML-EA approach for inverse optimization, followed by voxel printing and applications.

modulus and V_f is obtained from experiments. Here V_f represents the volume fraction of the hard material. Dog-bone tensile specimens with different V_f are fabricated using the commercial 3D printer Polyjet J750. Tensile tests are conducted using a uniaxial materials testing system (Instron 68SC-2) with a tensile rate of 5 mm/min. The experimental stress-strain curves are shown in Fig. 2(b). The Young's moduli with various V_f are obtained by linearly fitting the curves with a 5% strain. Material nonlinearity is neglected and geometric nonlinearity is accounted for. We choose 5% because the local strain of the material is generally less than 5%, even when the overall strain of the lattice structure is around 100% [26,47].

The relationship between Young's modulus and V_f is shown in Fig. 2(c). The voxel slices of the tensile specimens for $V_f = 0$ to 1 are also shown. Note that the rule of mixture has not been validated in multimaterial voxel 3D printing [48,49], even though it is effective in estimating the modulus of composites. The shrinkage ratios of the soft and hard materials are different in multimaterial voxel 3D printing, leading to complex interfacial bonding during UV curing, which could be one reason why the rule of mixture fails. The nonlinear dependence of the modulus on the volume fraction is a multidisciplinary problem involving the manufacturing process, chemical properties of the materials, and photoreaction dynamics, which is worthy of study [50].

The lattice shows a highly nonlinear behavior. The tangent modulus, the slope of the stress-strain curve at any specified stress or strain, is used to describe its effective modulus. The strain is obtained from dividing the displacement by the initial length of the lattice metamaterials. The stress is the nominal stresses and is calculated by $\sigma = F/A$, where F is applied force and A is the initial cross-section area of the lattice metamaterials [26,51].

The FEM is used to provide the database for the ML method. The ML method is a surrogate model to decrease the computational cost significantly. The EA

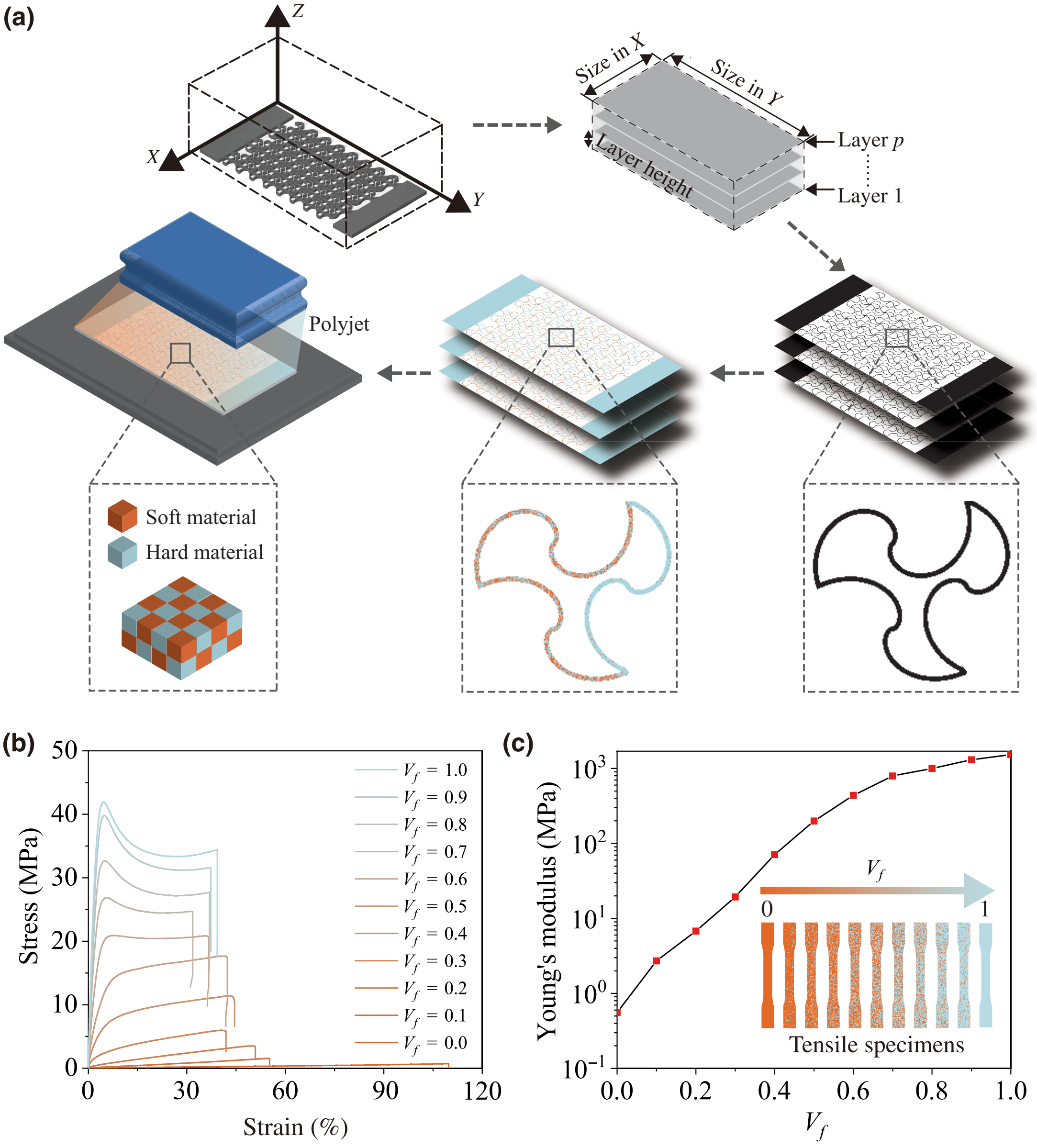

FIG. 2. (a) The manufacturing process of multimaterial lattice metamaterials using voxel printing. (b) The stress-strain curves of the tensile specimens with different volume fraction ratios of soft (Agilus) and hard (Veroblue) materials. V_f represents the volume fraction of the hard material. (c) Young's modulus as a function of V_f. The voxel slices of the tensile specimens with different V_f. The orange and blue colors represent the soft and hard materials, respectively.

is then integrated with ML to realize fast and efficient inverse optimizations. In detail, the FEM is first used to form the databases, including the strain-stress curves, stress-Poisson's ratio curves, and lateral profile curves of the lattice metamaterials. A PYTHON-assisted FEM model is developed to perform numerical analysis automatically, which overcomes the difficulties of exploring the broad design space and the tedious modeling process. The FEM is run through the commercial finite-element software ABAQUS (3DS Dassault Systèmes, France). Three-node quadratic hybrid beam elements are used with refined meshes to ensure computational accuracy. Next, the ANN-based ML model is established by learning the databases, which maps the nonlinear relationship between the design parameters and mechanical responses. Last, the EA method is combined with ML models to obtain optimal designs that satisfy the target mechanical response.

III. MACHINE LEARNING PREDICTION

In this section, we construct an ANN-based ML model to accurately predict the mechanical responses of

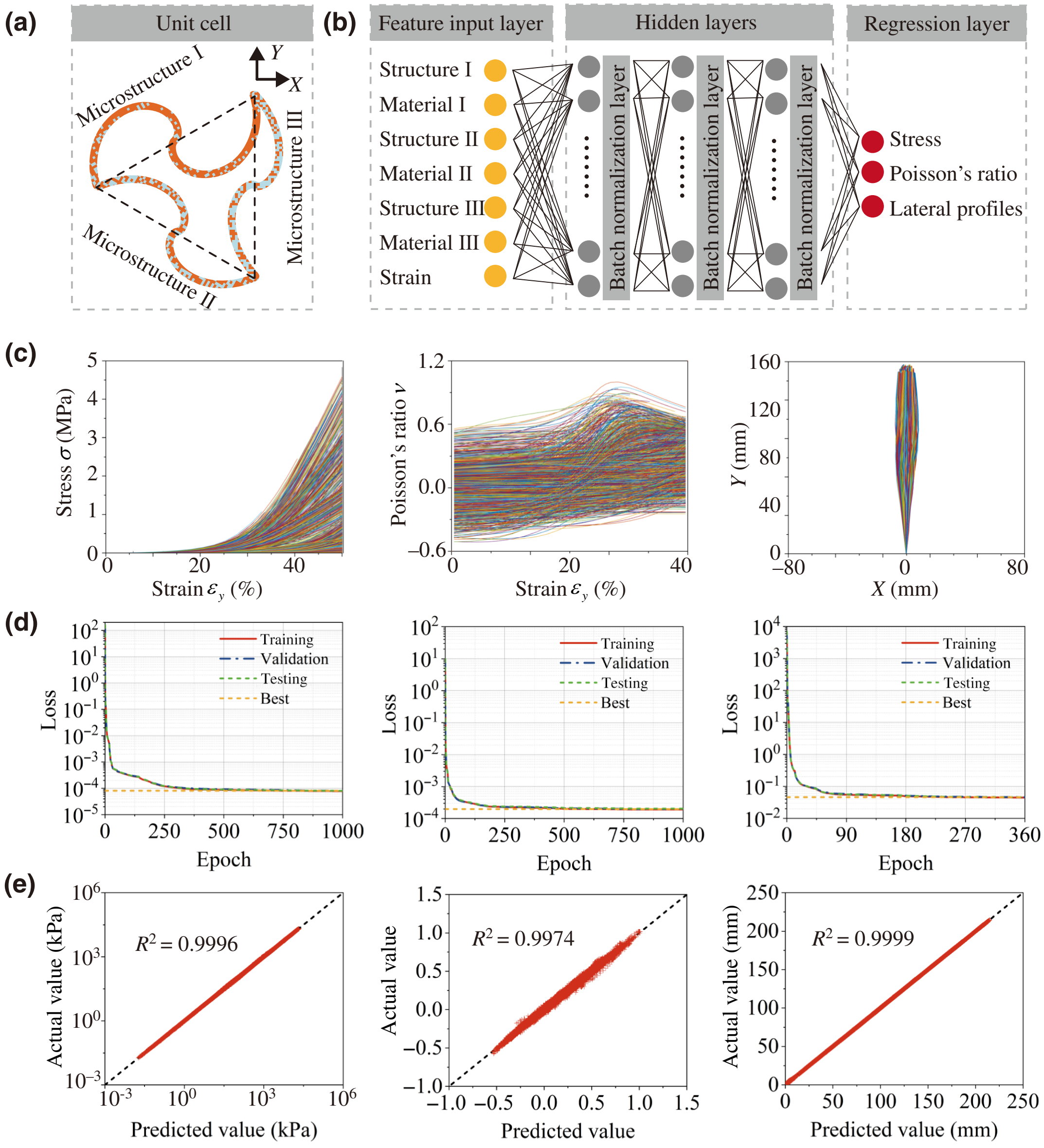

FIG. 3. The architecture and performance of the ANN-based ML model. (a) The typical unit cell constructed by microstructures I, II, and III. (b) ANN model composed of the feature input layer, the hidden layers, and the regression layer. (c) Databases for ML obtained by FEM simulation. Three mechanical properties, the stress-strain curves, Poisson's ratio-strain curves, and lateral profiles are studied. (d) The training, validation, and testing losses versus epochs during the training process of each database. (e) Comparisons of actual values and ML-predicted values for the stress-strain curves, Poisson's ratio-strain curves, and lateral profiles.

multimaterial lattice metamaterials under uniaxial tensile loadings. As shown in Fig. 3(a), a triangular unit consists of three microstructures (I, II, and III) with independent material properties and geometric designs. Therefore, the input data for ML include three parts: material and geometric parameters of the three microstructures, and the axial strain [Fig. 3(b)]. Three types of output data are considered: (1) tensile stress σ along the Y direction; (2) Poisson's ratio $\nu = -\varepsilon_x/\varepsilon_y$, where ε_x and ε_y are the strains in the X and Y directions; (3) the lateral profile of the deformed shape (details given in Fig. S5 within the Supplemental Material [46]). In cases (1) and (2), the metamaterials comprise 6×8 unit cells; the material and geometric parameters are the same for each periodic unit, though they may differ for each microstructure in the unit. In case (3), 6×10 unit cells are used and divided into three subregions; different subregions may have different material and geometric properties to enable diverse lateral profiles.

In each case, the mechanical responses of multimaterial lattice metamaterials are obtained using the PYTHON-assisted FEM model. Random geometric and material parameters within the range of Young's modulus ($E \in$ [0.5 MPa 1.5 GPa]) and geometric parameters ($n \in$ [1 3]) are used in the FEM model. The size of each database is chosen as 1750. In case (3), we set $n = 1$ for all the microstructures to simplify the database. All databases are further split into the training sets (70%), the validation sets (15%), and the test sets (15%).

Figure 3(c) shows the FEM-calculated stress-strain curves, Poisson's ratio-strain curves, and the lateral profiles. It can be seen that all multimaterial lattice metamaterials exhibit J-shaped strain-stress behaviors. The instant modulus increases with the applied strain due to the transformation from bending-dominated to tensile-dominated deformation of the microstructures. The variations in the structures and materials enable the vast design space for stiffness and Poisson's ratio. For example, the stress changes from around 2 to around 4680 kPa at $\varepsilon_y = 40\%$, and the Poisson's ratio varies from around −0.5 to 0.7. Lateral profiles can also be programmed by changing the material and geometric parameters in different subregions.

An ANN-based ML model is constructed to train and test databases using MATLAB. The network architecture consists of a feature input layer, the hidden layers, and a regression layer (details given in Table S1 within the Supplemental Material [46]). The hidden layers consist of three fully connected layers and batch normalization layers arranged alternately to accelerate the convergence speed and improve the stability of the model. The adaptive moment estimation (ADAM) optimizer is used to update hyperparameters to train the ANN, and the initial learning rate is 0.001. The rectified linear unit is used as the activation function between the hidden layer and the output layer to achieve nonlinear matching. Mean squared error (MSE) performs as the loss function to evaluate the accuracy of the ANN and is calculated by

$$l = \frac{1}{N}\sum_{i=1}^{N}(y_i - \hat{y}_i)^2, \tag{3}$$

where N is the number of the database, y_i is the actual value, and $\hat{y}_i$ is the corresponding predicted value. The loss function is used to evaluate the accuracy of the ML model and as feedback to improve the model. Figure 3(d) shows the training, validation, and testing losses versus epochs during the training process of each database. An "epoch" implies one complete process of training the database and updating the model parameters. The process is computed using one central processing unit (CPU, Intel Core i7 10700) and one graphics processing unit (GPU, NVIDIA GeForce RTX 3060). The loss functions all converge to a steady state. The predicted and actual values are consistent with high coefficients of determination ($R^2 = 0.9996$, 0.9974, and 0.9999), indicating the reasonably high prediction accuracy of the established ML model [Fig. 3(e)]. The ML predictions have much higher efficiency than FEM simulations as depicted in Table I, reducing the elapsed time from hours to seconds.

TABLE I. Time cost for 1750 predictions with ML (ANN) and FEM (estimated). The process is based on one CPU core (Intel Core i7-10700) and one GPU (NVIDIA GeForce RTX 3060).

Time cost for 1750 predictions		
Data	ML (s)	FEM (h)
Strain-stress	7.1	∼72.9
Strain-Poisson's ratio	7.3	∼72.9
Strain-shape profiles	8.6	∼78.3

IV. MACHINE LEARNING-EVOLUTIONARY ALGORITHM OPTIMIZATION

The ML model is further combined with the EA to realize the inverse design of target responses. The EA is a biomimetic optimization algorithm inspired by natural selection that simulates the behavior of biological populations. As schematically illustrated in Fig. 4(a), the algorithm begins by creating a random initial population, including 200 reasonably distributed individuals. The geometric and material parameters should satisfy the following two constraints: (1) the geometric parameter n is set to [1 3] to avoid self-intersection; (2) the material parameter E is set to [0.5 MPa 1.5 GPa], which is the range that can be achieved in experiments. Each individual is a multimaterial lattice metamaterial constructed with random material and geometric parameters. The algorithm then iteratively updates the population using the following procedures.

First, each individual is scored by calculating the current fitness value. The fitness function for a single target is set as

$$F_1 = \sqrt{\frac{1}{k}\sum_{i=1}^{k}(y_1(x_i) - \hat{y}_1(x_i))^2}, \tag{4}$$

where k is the number of process goals to be satisfied. x_i are vectors that contain parameters including material and structural properties (constant to be optimized), and applied strain (variation). $y_1(x_i)$ are the target values and $\hat{y}_1(x_i)$ are the predicted values obtained by the ML model. When performing m multitarget optimizations throughout the process continuously, Eq. (4) changes to

$$F_m = \sqrt{\sum_{j=1}^{m}\left[\frac{1}{k_j}\sum_{i=1}^{k_j}(y_j(x_i) - \hat{y}_j(x_i))^2\right]}, \tag{5}$$

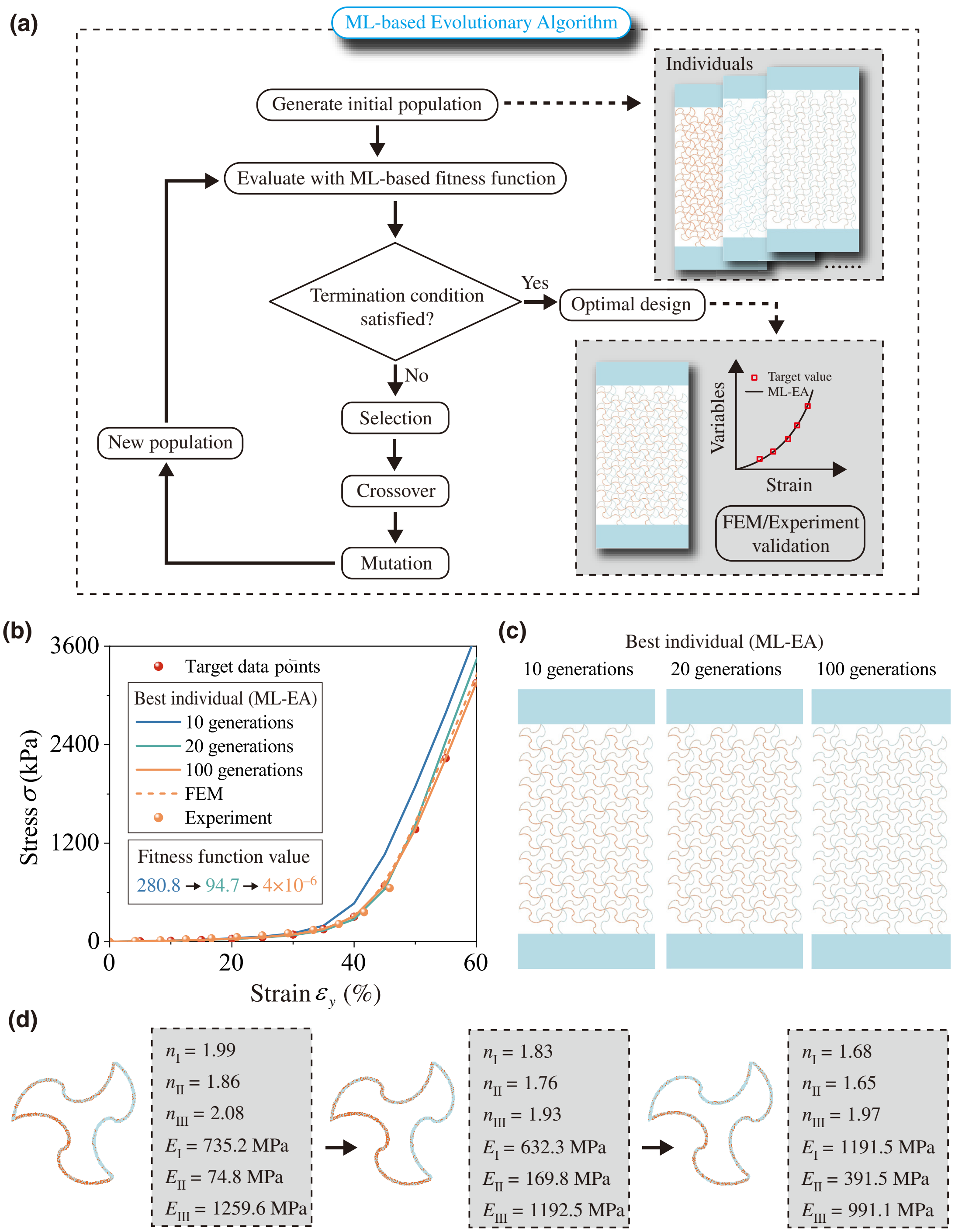

FIG. 4. (a) Schematic illustration of the ML-EA optimization approach. (b) The strain-stress matching process for target data points. (c) The voxel matrixes of the best individuals of 10, 20, and 100 generations. (d) The corresponding unit cells and the design parameters.

where k_j is the number of process goals for the jth target, $y_j(x_i)$ are the target values, and $\hat{y}_j(x_i)$ are the corresponding predicted values.

Next, the parents and elite subpopulations are selected according to the fitness value. Elite individuals are passed to the next population to form the next generation, while new individuals are generated by parents through crossover and mutation. The iterations stop when the minimum fitness function value is less than or equal to a limitation (10^{-5}) in the current population or the number of generations reaches 800. The optimal results are the material and geometric parameters corresponding to the best individual. The ML-EA approach helps to efficiently explore the myriad of possible designs and identify the optimal structural and material parameters, resulting in target mechanical responses.

As depicted in Fig. 4(b), we demonstrate a strain-stress matching process for target data points. The fitness function values of the best individuals of 10 and 100 generations decrease from 280.8 to 4×10^{-6}, which satisfies the termination condition. The optimal results based on the ML-EA approach agree well with the target values, FEM simulation, and experiments. The lattice metamaterials are fabricated using the optimal parameters obtained. The experimental, FEM-simulated, and ML-EA-predicted stress-strain curves are shown in Fig. S3(a) within the Supplemental Material [46]. The deformed shapes in the experiments and the FEM simulations are compared in Fig. S3(b) within the Supplemental Material [46]. It can be observed that both the deformed shapes and the stress-strain curves show good agreement. Figure 4(c) shows the voxel matrixes of the best individuals of 10, 20, and 100 generations. The corresponding unit cells and the design parameters are shown in Fig. 4(d).

V. APPLICATION PROSPECTS

A. Bionic mechanical behavior matching

Many biological tissues have natural J-shaped strain-stress curves due to the curved and chained microstructures (e.g., collagen fibril and fiber) that help them avoid excessive strain. Lattice metamaterials that can reproduce nonlinear mechanical behaviors of biological tissues and organs are essential to avoid mechanical damage caused by biointegrated devices. Using the ML-EA approach, multimaterial lattice metamaterials can accurately realize J-shaped stiffness matching in the broad design space (from kilopascals to megapascals).

As shown in Fig. 5(a), the internal mammary artery, lens capsule, and rat myocardium all have J-shaped strain-stress mechanical behavior (data from Refs. [52,53]). The experimental mechanical responses of three biological tissues under uniaxial loading are uniformly sampled. The sampled points are used as targets in the ML-EA approach. The results show that the optimally designed multimaterial lattice metamaterials can replicate the target J-shaped strain-stress curves. The FEM simulations are conducted using

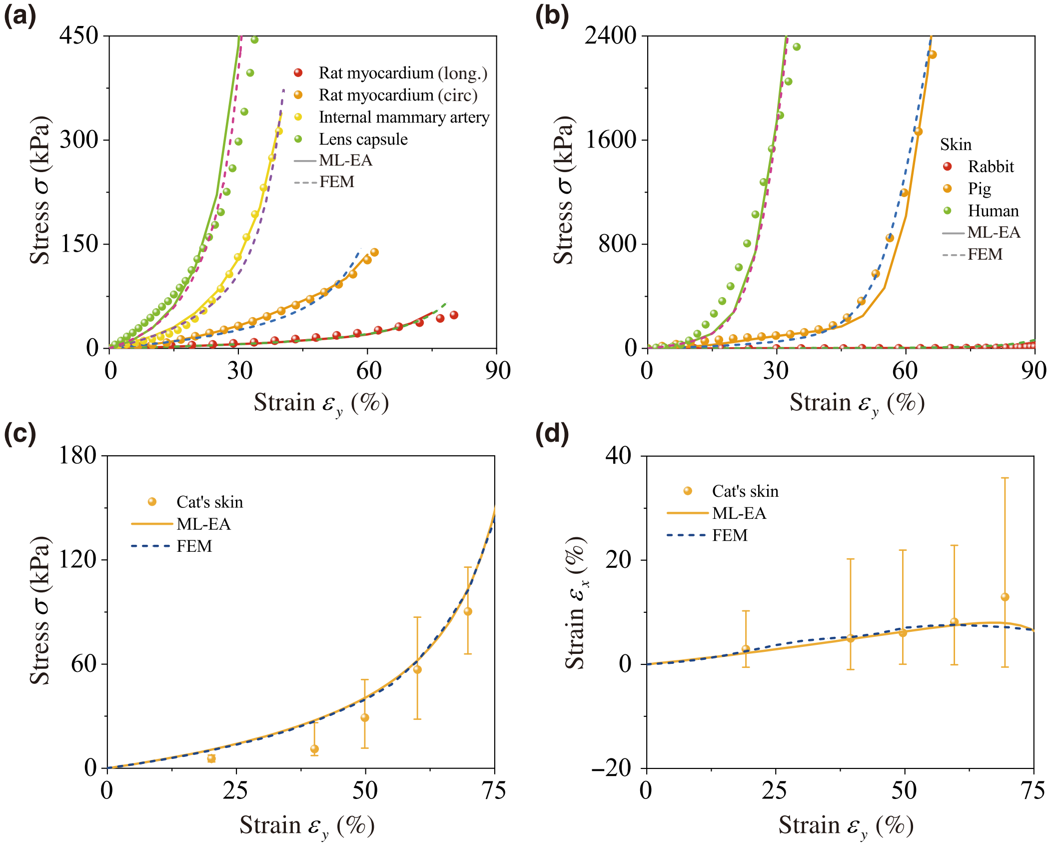

FIG. 5. Bionic mechanical behavior matching. (a),(b) The ML-EA optimal designs accurately match the J-shaped strain-stress curves of various biological tissues and organs. FEM simulations are used as verification. (c),(d) The nonlinear responses of transverse strains and stress of cat's skin can be simultaneously reproduced by the optimal multimaterial lattice metamaterial using the ML-EA approach.

the optimized parameters and verify the accuracy. Note that rat myocardium has anisotropic mechanical behaviors, and both circumferential and longitudinal stress-strain curves are reproduced by the inverse designs. Detailed design parameters and voxel slices are shown in Table S2 and Figs. S4(a)–S4(d) within the Supplemental Material [46].

The strain-stiffening effects of the rabbit, pig, and human skin are also fitted in Fig. 5(b) (data from Refs. [53,54]). The corresponding uniaxial tensile experimental results show the apparent discrepancy in strain-stress curves ($\sigma =$ $\sim$0.5, $\sim$ 100, and $\sim$ 1700 kPa at $\varepsilon_y = 30\%$, respectively). Using the ML-EA approach, the optimal results agree reasonably well with the actual and FEM-simulated uniaxial tensile curves [details given in Table S3 and Figs. S4(e)–S4(g) within the Supplemental Material [46]].

The controllable Poisson effect is of practical interest in tissue engineering and stretchable electronics. However, both stress and Poisson's ratio have a complex coupling relationship with strain, posing difficulties in developing metamaterials that match multitarget mechanical responses. The optimal design shown in Figs. 5(c) and 5(d) can simultaneously exhibit the nonlinear strain-stress and strain-Poisson's ratio curves of cat skin. The optimization progress is performed through approximately 600 generations of evolution using the ML-EA method by setting a two-target fitness function [details given in Table S3 and Figs. S4(h) within the Supplemental Material [46]], which requires roughly 120 000 evaluations of different material and structural parameters. The ML-EA approach achieves the optimal design in around 3.4 min, while the time cost is expected to be around 5000 h using the FEM-EA approach (including 120 000 FEM predictions).

B. Programmable shape matching

Programmable shape matching structures have shown promising applications in soft robots, deployable systems, and wearable medical devices. Fast and accurate shape matching can be achieved via the optimal subregional design of the multimaterial lattice metamaterial. Figures 6(a)–6(c) show the ML-predicted and FEM-simulated lateral profiles of three typical lattice metamaterials at $\varepsilon_y =$ 40%. The FEM deformed shapes are given in Fig. 6(d). The voxel slices of the three lattice metamaterials are shown in Figs. S6(a)–S6(c) of the Supplemental Material [46]. The ML-predicted and FEM-simulated lateral profiles agree well, indicating the promising ability to match undulating shapes using the ML-EA approach.

We demonstrate an example of matching a porcelain vase's lateral profile. The optimization is set as 2D. We start by binarizing the porcelain vase image to improve the contrast. After noise reduction, the boundary contour is extracted using ImageJ software. The target lateral profile is then generated by sampling, as shown in Fig. 6(e) (details given in Fig. S7 within the Supplemental Material [46]). The fitness function is defined as

TABLE II. Time cost for ML-EA optimization and FEM (estimated). The process is based on one CPU core (Intel Core i7-10700) and one GPU (NVIDIA GeForce RTX 3060).

Time cost for ML-EA optimization		
Design	ML-EA (min)	FEM (h)
Cat's skin	3.4 ($\sim$600 generations)	$\sim$5000
Shape edge of the porcelain	6.5 ($\sim$750 generations)	$\sim$6250

$$F_1 = \sqrt{\frac{1}{k}\sum_{i=1}^{k}(x_i - \hat{x}_i)^2}, \tag{6}$$

where x_i and $\hat{x}_i$ are the ith actual and ML-predicted X coordinates at $\varepsilon_y = 40\%$ [Fig. 6(f)]. Here, the fitness function describes how close the optimized lateral profile is to the target one. As shown in Fig. 6(g), the deformed lateral profile of the optimal design agrees well with those of the porcelain vase and the FEM-simulated results [details given in Table S4 and Fig. S6(d) within the Supplemental Material [46]]. Based on the optimal material and geometric parameters, the lattice metamaterials are 3D voxel printed. The optical image of the printed lattice metamaterials at $\varepsilon_y = 40\%$ under a uniaxial loading is shown in Fig. 6(i), which visually illustrates the accurate agreement of the lateral profiles (see Supplemental Material Video S1 [46]). FEM simulation is conducted for comparison [Fig. 6(h)]. As shown in Table II, the ML-EA approach completes the optimization process in 6.5 min, which significantly saves the time cost compared with the FEM-EA approach (about 6250 h). During the optimization, we set the geometric parameters n for all the microstructures as 1 and the material parameters in the triangular units in one region as the same to reduce the computational cost in optimization. However, the lattice metamaterial filling the optimal shape looks discontinuous owing to this simplification [Fig. 6(i)]. The continuity can be increased by using more independent design parameters, but the computation cost is increased simultaneously.

VI. DISCUSSION

A. Design space

The incorporation of material distribution and geometric design enlarges the design space of the lattice metamaterials. As depicted in Fig. S8 within the Supplemental Material [46], we compare the design spaces of mechanical responses constructed in three ways: (1) tuning the material while fixing the geometry ($n = 1$); (2) tuning the geometry while fixing the material ($E = 1500$ kPa); (3) tuning the material and geometry simultaneously. Broader design spaces of both strain-stress curves and

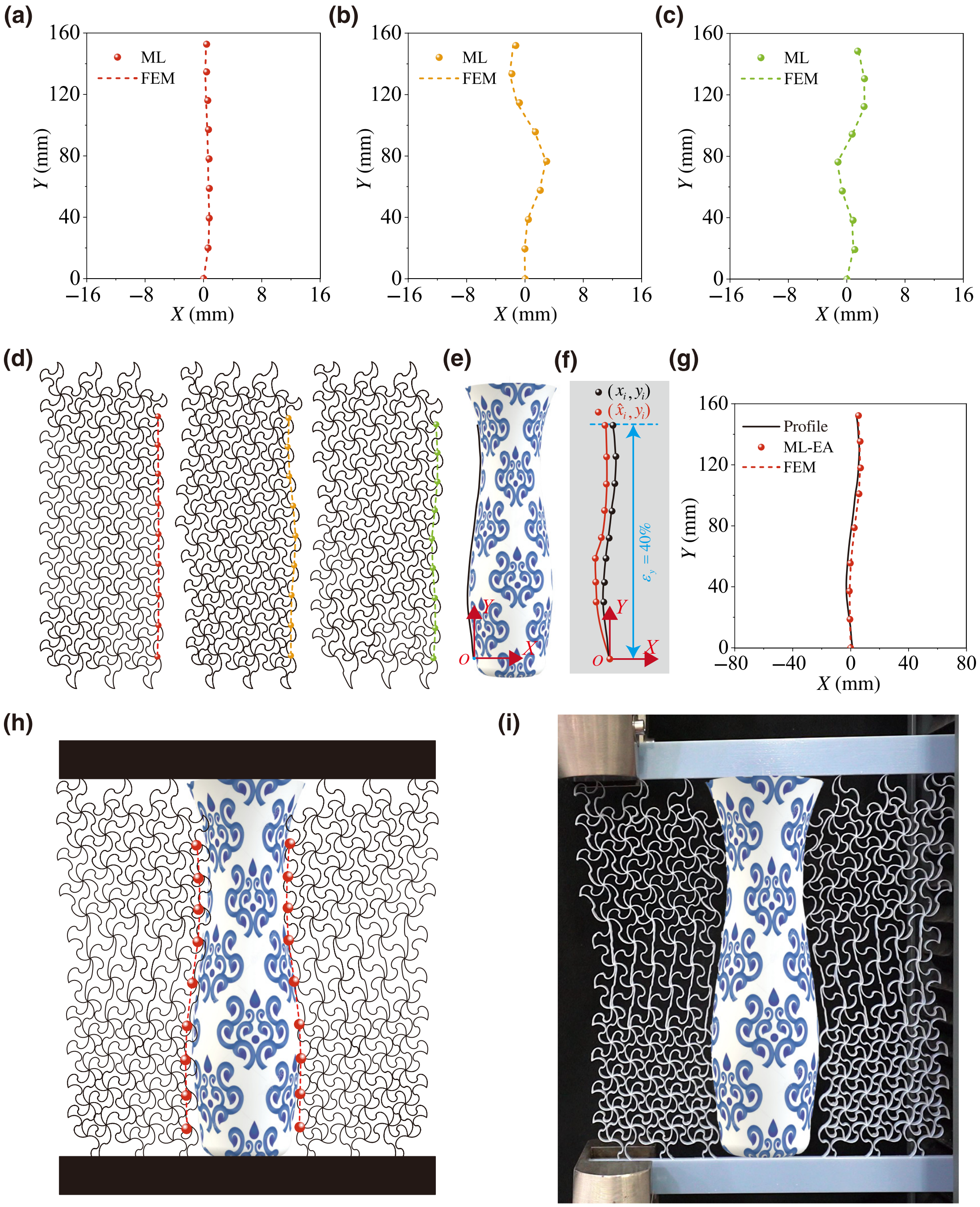

FIG. 6. Programmable shape matching. (a)–(c) Three typical deformed lateral profiles of ML predictions and FEM simulations at $\varepsilon_y = 40\%$. (d) The corresponding FEM results. (e) The lateral profile of a porcelain vase is selected as the target. (f) The fitness function is formed by relating the actual [black dots (x_i, y_i)] and ML-predicted [red dots $(\hat{x}_i, y_i)$] coordinates of nine sampling points. (g) Comparison of the actual, ML-EA-optimized, and FEM-simulated lateral profiles. (h) FEM results and (i) optical images of deformed optimal design.

strain-Poisson’s ratio curves are enabled by simultaneously programming the material distributions and geometric parameters. For instance, the stress variation ranges for each design space at $\varepsilon_y = 10\%$ are 0.4–6.0, 6.1–53.5, and 0.4–53.5 MPa, respectively. Meanwhile, the tunable domains of Poisson’s ratio are −0.25 to 0.28, −0.27 to 0.15, and −0.51 to 0.65. It is worth noting that almost all data points in the design space can be obtained due to the continuous adjustment of design parameters.

The low cost of the ML model enables the exploration of each microstructure's role on the total mechanical behaviors of the lattice metamaterials. Figures S9 and S10 in the Supplemental Material [46] show the effects on the stresses and Poisson's ratios by tuning each microstructure's material and structural parameters when $\varepsilon_y = 20\%$ and 40%. It can be observed that the stress increases with decreasing structural curling (n from 1 to 3) and increasing Young's modulus (E from 100 to 1500 kPa) for each microstructure. The tunable range of stress is 3–160 kPa at $\varepsilon_y = 20\%$ and 10–2600 kPa at $\varepsilon_y = 40\%$ for microstructure III, while the ranges are significantly limited for microstructures I and II. This indicates that microstructure III undertakes the primary tensile deformation.

Furthermore, an increasing Young's modulus of microstructure I leads to a decreasing Poisson's ratio from a positive maximum (0.27 at $\varepsilon_y = 20\%$ and 0.29 at $\varepsilon_y = 40\%$) to around zero, while the structural parameter of microstructure I has a negligible effect on it. The Poisson's ratio increases from a negative value to a positive value as n and E of microstructure II increase. For example, it changes from -0.25 to 0.12 at $\varepsilon_y = 20\%$ and from -0.25 to 0.15 at $\varepsilon_y = 40\%$. In contrast, the Poisson's ratio decreases from 0.1 to -0.18 at $\varepsilon_y = 20\%$ and increases from 0.1 to 0.35 at $\varepsilon_y = 40\%$ with the increase of n and E of microstructure III. These opposite trends in the change of Poisson's ratio may result from the transformation from bending-dominated to tensile-dominated deformation.

B. Mechanism of J-shaped stress-strain responses

Both the microstructures and the lattice metamaterials show J-shaped stress-strain responses resulting from the structural design of the metamaterials. The J-shaped stress-strain response of the microstructures is due to the transition from bending-dominated to tension-dominated deformation. The mechanical behavior of a microstructure is typically characterized by two different stages. The curved microstructure bends and uncurls at the first stage, leading to a relatively low modulus. In the second stage, the microstructure is nearly straightened, and tension dominates the deformation with further increased applied strain, leading to a sharp increase in the tangent modulus. The J-shaped stress-strain response of the lattice metamaterials results from the mechanical behaviors of the three microstructures in a periodic unit. Figure S11(c) within the Supplemental Material [46] exhibits the FEM-simulated deformed shapes of a lattice metamaterial and a periodic unit at strain $\varepsilon_y = 0$, 15%, 30%, and 45%. The color maps show the local principal strain in the periodic unit. All three microstructures exhibit bending-dominated deformation initially, leading to a low stiffness. As the strain increases (around 45%), tension dominates the deformations of microstructures II and III, resulting in a sharp rise in the stiffness.

C. Mechanism of tunable Poisson's ratio

The designed metamaterials show tunable Poisson's ratio by virtue of the microstructures. The Poisson's ratio of lattice metamaterials is determined by both the geometric configurations and the material properties of the three microstructures in a periodic unit. We study the effects on Poisson's ratios by tuning the material parameters E and geometric parameters n of each microstructure at a 20% strain in Fig. S9 within the Supplemental Material [46]. Based on the contour map, we can draw the following conclusions qualitatively:

(1) if microstructure I is much stiffer than microstructure II, the lattice shows a negative Poisson's ratio;

(2) if microstructure I is much softer than microstructure II, the lattice shows a positive Poisson's ratio;

(3) if the stiffness of the microstructure I and II are comparable, the lattice exhibits a nearly zero Poisson's ratio.

These conclusions are based on the following reasons. A vertical force is applied on the left node of the periodic unit when the lattice is under tension, which can be decomposed into a compression force on microstructure I and a tensile force on microstructure II [Fig. S12(a) within the Supplemental Material [46]]. If microstructure I is much stiffer, microstructure II is elongated and microstructure I retains its original length. The left node has to move toward the top-left to satisfy the geometric compatibility [Fig. S12(b) within the Supplemental Material [46]], and the lattice shows a negative Poisson's ratio (conclusion 1). In contrast, microstructure I is compressed if it is much softer, the left node moves toward the top-right [Fig. S12(c) within the Supplemental Material [46]] and the lattice shows a positive Poisson's ratio (conclusion 2).

FEM simulations are conducted to validate the above mechanism. As the stiffness of the microstructure is determined by both the geometric and material parameters, we study the effect of geometric and material parameters separately. Figure S13 within the Supplemental Material [46] shows the effect of geometric parameters. Three different structures are shown. Note that a microstructure with a larger n is softer. The same material $E = 1.5$ GPa is used. The FEM-simulated deformed shapes of the lattice metamaterials and the representative unit at $\varepsilon_y = 20\%$ are plotted in Figs. S13(d)–S13(f) within the Supplemental Material [46]. Lattices (a), (b), and (c) exhibit a negative, nearly zero, and positive Poisson's ratio, respectively. In lattice (a), microstructure I ($n_{\mathrm{I}} = 3$) is much stiffer than microstructure II ($n_{\mathrm{II}} = 1$). Microstructure II elongates and microstructure I remains the original length under tension. The left node moves toward the top-left, and the lattice shows a negative Poisson's ratio, (conclusion 1). In lattice (c), microstructure I is much softer and compressed. Lattice (c) exhibits a positive Poisson's ratio (conclusion 2).

For lattice (b), the initial stiffness of microstructures I and II are comparable, and the lattice metamaterials exhibit a nearly zero Poisson's ratio (conclusion 3).

Similarly, Fig. S14 within the Supplemental Material [46] studies the effect of the material parameters on the initial Poisson's ratio. The same geometries are used for each microstructure, while different material parameters are used. The FEM-simulated deformed shapes of the lattice metamaterials and the periodic unit at $\varepsilon_y = 20\%$ are plotted in Figs. S14(d)–S14(f) in the Supplemental Material [46]. It can be observed that lattices (a), (b), and (c) exhibit a negative, nearly zero, and positive Poisson's ratio, respectively, which can also be explained by the conclusions presented previously.

The transition from bending-dominated to tension-dominated response (the J-shaped stress-strain curves) is a mechanism responsible for the change of the behaviors of the Poisson's ratio. Figure S11(b) within the Supplemental Material [46] plots the Poisson's ratios of a lattice structure at four different strains $\varepsilon_y = 0$ (marker i), 15% (marker ii), 30% (marker iii), and 45% (marker iv). It can be seen that the Poisson's ratio is nearly 0 at markers i to iii, while it increases to around 0.3 at marker iv. The corresponding stress-strain relationships at markers i to iv are also marked in Fig. S11(a) within the Supplemental Material [46]. When ε_y is small (markers i to iii), the stiffness of microstructures I and II are comparable and the Poisson's ratio is around 0, based on conclusion 3 about the Poisson's ratio. At $\varepsilon_y = 45\%$, the stiffness of microstructure II increases significantly due to the J-shaped stress-strain curves [marker iv in Fig. S11(a) within the Supplemental Material [46]], while the stiffness of microstructure I does not increase much as it is compressed. Therefore, microstructure II becomes much stiffer than microstructure I, leading to a sharp positive increase in the Poisson's ratio based on conclusion 2.

Note that the Poisson's ratio of the lattice metamaterials is a complex phenomenon involving the nonlinear response of the microstructures and geometric patterns of the lattice metamaterials. Here, we only intend to provide a qualitative explanation for understanding. Accurately predicting the Poisson's ratio and understanding its underlying mechanism requires a detailed calculation of the instantaneous moduli of the microstructures, the changing geometric configurations, and force transmission inside the lattice structures.

D. Computational costs

The developed ML model demonstrates high efficiency and accuracy in the forward prediction of multimaterial lattice metamaterials, ensuring the rapid inverse design for the desired mechanical responses when combined with the EA method. Although the generation of ML databases requires thousands of FEM simulations, the time cost is much lower than the iterative optimization process of traditional FEM-EA methods (Tables I and II). The computation time of one evaluation is around 2.5 min for the FEM simulation, computing with one CPU core (Intel Core i7-10700) and one GPU (NVIDIA GeForce RTX 3060). In the optimal design for the cat's skin, the optimization process requires around 600 generations and each generation includes 200 evaluations. Therefore, the time consumed using the FEM simulation is 600 × 200 × ∼2.5 min = ∼5000 h. Similarly, the optimization process requires around 750 generations to reproduce the shape edge of the porcelain vase, so the estimated consumed time is 750 × 200 × ∼2.5 min = ∼6250 h. Once the ML model is established, further FEM simulations are barely needed in the subsequent computations. Moreover, the ML model is convenient in reconstructing multitarget fitness functions.

It should be noted that the developed design approach is a general framework for the design of multimaterial mechanical metamaterials. In this work, a particular curvature function $R(\alpha) = \alpha^n (n \in [1\ 3])$ is used to construct the microstructure; a triangular lattice pattern is used and the materials' stiffness varies by around 3 orders. The design and optimizations of lattice metamaterials with diverse microstructures (such as waving, curling, or spiral shapes) and combining with other types of lattice patterns and stiffness-tunable material systems can also be conducted using the proposed framework. The intrinsic chirality shape of $R(\alpha) = \alpha^n$ makes the problem more complicated due to its rotational behavior under axial loading, especially compared with the widely used horseshoe structures with constant curvatures. In our previous study [28], we developed a combined theoretical, numerical, and experimental method to study the mechanical behaviors of lattice metamaterials constructed from an arbitrarily curved microstructure. The mechanical performance of the lattice structures built from the microstructure can be easily analyzed using the established method with a negligible increase in computational cost.

VII. CONCLUSION

In summary, we propose a digital design workflow for multimaterial lattice metamaterials and develop a multitarget optimization method based on ML and the EA. The digital voxel models are generated by integrating the material distribution and geometric design of microstructures. The 3D voxel printing is used to fabricate the multimaterial lattice metamaterials with tremendous design potential. For fast and precise prediction of mechanical responses, an ANN-based ML model is trained using the database formed by a PYTHON-assisted FEM model. The ML model achieves accurate prediction of strain-stress curves, strain-Poisson's curves, and deformed lateral profiles ($R^2 = 0.9996, 0.9974, \text{and}\ 0.9999$). The optimal designs that match multitarget mechanical behaviors can be efficiently found by combining the ML model and EA method. Note that the time cost of optimization using the developed ML-EA approach is reduced from thousands of hours to minutes compared with the FEM-EA approach. Using the design workflow and the ML-EA approach, the J-shaped strain-stress curves of various biological tissues and organs can be accurately reproduced. Moreover, the stiffness and Poisson's ratio of cat skin can be simultaneously matched by modifying the fitness function to perform the ML-EA approach. The design strategy can be used for programable shape matching, and we demonstrate an optimized design process that automatically mimics the lateral profile of a porcelain vase. This work can aid the design and optimization of multimaterial mechanical metamaterials and holds promising potential in stretchable flexible electronics and soft robotics.

ACKNOWLEDGMENT

D.W. acknowledges support from the National Natural Science Foundation of China (Grant No. 51905336) and the State Key Laboratory of Mechanical System and Vibration (Grant No. MSVZD202212).

[1] K. Bertoldi, V. Vitelli, J. Christensen, and M. Van Hecke, Flexible mechanical metamaterials, Nat. Rev. Mater. **2**, 1 (2017).

[2] B. Florijn, C. Coulais, and M. van Hecke, Programmable Mechanical Metamaterials, Phys. Rev. Lett. **113**, 175503 (2014).

[3] T. Frenzel, M. Kadic, and M. Wegener, Three-dimensional mechanical metamaterials with a twist, Science **358**, 1072 (2017).

[4] X. Zheng, H. Lee, T. H. Weisgraber, M. Shusteff, J. DeOtte, E. B. Duoss, J. D. Kuntz, M. M. Biener, Q. Ge, and J. A. Jackson, Ultralight, ultrastiff mechanical metamaterials, Science **344**, 1373 (2014).

[5] T. Chen, M. Pauly, and P. M. Reis, A reprogrammable mechanical metamaterial with stable memory, Nature **589**, 386 (2021).

[6] A. J. D. Shaikeea, H. Cui, M. O'Masta, X. R. Zheng, and V. S. Deshpande, The toughness of mechanical metamaterials, Nat. Mater. **21**, 297 (2022).

[7] G. Librandi, E. Tubaldi, and K. Bertoldi, Programming nonreciprocity and reversibility in multistable mechanical metamaterials, Nat. Commun. **12**, 1 (2021).

[8] M. Mohsenizadeh, F. Gasbarri, M. Munther, A. Beheshti, and K. Davami, Additively-manufactured lightweight Metamaterials for energy absorption, Mater. Des. **139**, 521 (2018).

[9] X. Zhao, G. Duan, K. Wu, S. W. Anderson, and X. Zhang, Intelligent metamaterials based on nonlinearity for magnetic resonance imaging, Adv. Mater. **31**, 1905461 (2019).

[10] Q. Ge, Z. Chen, J. Cheng, B. Zhang, Y.-F. Zhang, H. Li, X. He, C. Yuan, J. Liu, and S. Magdassi, 3D printing of highly stretchable hydrogel with diverse UV curable polymers, Sci. Adv. **7**, eaba4261 (2021).

[11] Z. Liu, M. A. Meyers, Z. Zhang, and R. O. Ritchie, Functional gradients and heterogeneities in biological materials: Design principles, functions, and bioinspired applications, Prog. Mater. Sci. **88**, 467 (2017).

[12] Z. Liu, Y. Zhu, D. Jiao, Z. Weng, Z. Zhang, and R. O. Ritchie, Enhanced protective role in materials with gradient structural orientations: Lessons from nature, Acta Biomater. **44**, 31 (2016).

[13] B. Zhang, Q. Han, J. Zhang, Z. Han, S. Niu, and L. Ren, Advanced bio-inspired structural materials: Local properties determine overall performance, Mater. Today **41**, 177 (2020).

[14] V. Imbeni, J. Kruzic, G. Marshall, S. Marshall, and R. Ritchie, The dentin–enamel junction and the fracture of human teeth, Nat. Mater. **4**, 229 (2005).

[15] S. P. Ho, B. Yu, W. Yun, G. W. Marshall, M. I. Ryder, and S. J. Marshall, Structure, chemical composition and mechanical properties of human and rat cementum and its interface with root dentin, Acta Biomater. **5**, 707 (2009).

[16] P. Fratzl, H. S. Gupta, F. D. Fischer, and O. Kolednik, Hindered crack propagation in materials with periodically varying Young's modulus—lessons from biological materials, Adv. Mater. **19**, 2657 (2007).

[17] J. C. Weaver, G. W. Milliron, A. Miserez, K. Evans-Lutterodt, S. Herrera, I. Gallana, W. J. Mershon, B. Swanson, P. Zavattieri, and E. DiMasi, The stomatopod dactyl club: A formidable damage-tolerant biological hammer, Science **336**, 1275 (2012).

[18] S. Amini, A. Masic, L. Bertinetti, J. S. Teguh, J. S. Herrin, X. Zhu, H. Su, and A. Miserez, Textured fluorapatite bonded to calcium sulphate strengthen stomatopod raptorial appendages, Nat. Commun. **5**, 1 (2014).

[19] M. Rafiee, R. D. Farahani, and D. Therriault, Multi-material 3D and 4D printing: a survey, Adv. Sci. **7**, 1902307 (2020).

[20] M. J. Prajapati, A. Kumar, S.-C. Lin, and J.-Y. Jeng, Multi-material additive manufacturing with lightweight closed-cell foam-filled lattice structures for enhanced mechanical and functional properties, Addit. Manuf. **54**, 102766 (2022).

[21] C. Bader, D. Kolb, J. C. Weaver, S. Sharma, A. Hosny, J. Costa, and N. Oxman, Making data matter: Voxel printing for the digital fabrication of data across scales and domains, Sci. Adv. **4**, eaas8652 (2018).

[22] M. A. Skylar-Scott, J. Mueller, C. W. Visser, and J. A. Lewis, Voxelated soft matter via multimaterial multinozzle 3D printing, Nature **575**, 330 (2019).

[23] Z. Han and K. Wei, Multi-material topology optimization and additive manufacturing for metamaterials incorporating double negative indexes of Poisson's ratio and thermal expansion, Addit. Manuf. **54**, 102742 (2022).

[24] J. Morris, W. Wang, D. Shah, T. Plaisted, C. J. Hansen, and A. V. Amirkhizi, Expanding the design space and optimizing stop bands for mechanical metamaterials, Mater. Des. **216**, 110510 (2022).

[25] J. W. Boley, W. M. Van Rees, C. Lissandrello, M. N. Horenstein, R. L. Truby, A. Kotikian, J. A. Lewis, and L. Mahadevan, Shape-shifting structured lattices via multimaterial 4D printing, Proc. Natl. Acad. Sci. U. S. A. **116**, 20856 (2019).

[26] Q. Ma, H. Cheng, K.-I. Jang, H. Luan, K.-C. Hwang, J. A. Rogers, Y. Huang, and Y. Zhang, A nonlinear mechanics model of bio-inspired hierarchical lattice materials consisting of horseshoe microstructures, J. Mech. Phys. Solids **90**, 179 (2016).

[27] J. Liu, D. Yan, and Y. Zhang, Mechanics of unusual soft network materials with rotatable structural nodes, J. Mech. Phys. Solids **146**, 104210 (2021).

[28] L. Dong, D. Wang, J. Wang, C. Jiang, H. Wang, B. Zhang, M. S. Wu, and G. Gu, Modeling and Design of Periodic Polygonal Lattices Constructed from Microstructures with Varying Curvatures, Phys. Rev. Appl. **17**, 044032 (2022).

[29] N. Karathanasopoulos, H. Reda, and J.-f. Ganghoffer, Designing two-dimensional metamaterials of controlled static and dynamic properties, Comput. Mater. Sci. **138**, 323 (2017).

[30] K. ElNady, I. Goda, and J.-F. Ganghoffer, Computation of the effective nonlinear mechanical response of lattice materials considering geometrical nonlinearities, Comput. Mech. **58**, 957 (2016).

[31] N. Karathanasopoulos, F. Dos Reis, H. Reda, and J.-F. Ganghoffer, Computing the effective bulk and normal to shear properties of common two-dimensional architectured materials, Comput. Mater. Sci. **154**, 284 (2018).

[32] X. Ni, X. Guo, J. Li, Y. Huang, Y. Zhang, and J. A. Rogers, 2D mechanical metamaterials with widely tunable unusual modes of thermal expansion, Adv. Mater. **31**, 1905405 (2019).

[33] C. M. Hamel, D. J. Roach, K. N. Long, F. Demoly, M. L. Dunn, and H. J. Qi, Machine-learning based design of active composite structures for 4D printing, Smart Mater. Struct. **28**, 065005 (2019).

[34] T. Erps, M. Foshey, M. K. Luković, W. Shou, H. H. Goetzke, H. Dietsch, K. Stoll, B. von Vacano, and W. Matusik, Accelerated discovery of 3D printing materials using data-driven multiobjective optimization, Sci. Adv. **7**, eabf7435 (2021).

[35] L. G. Wright, T. Onodera, M. M. Stein, T. Wang, D. T. Schachter, Z. Hu, and P. L. McMahon, Deep physical neural networks trained with backpropagation, Nature **601**, 549 (2022).

[36] C. Wang, X. Tan, S. Tor, and C. Lim, Machine learning in additive manufacturing: State-of-the-art and perspectives, Addit. Manuf. **36**, 101538 (2020).

[37] J. G. Freeze, H. R. Kelly, and V. S. Batista, Search for catalysts by inverse design: Artificial intelligence, mountain climbers, and alchemists, Chem. Rev. **119**, 6595 (2019).

[38] B. Kim, S. Lee, and J. Kim, Inverse design of porous materials using artificial neural networks, Sci. Adv. **6**, eaax9324 (2020).

[39] P. Z. Hanakata, E. D. Cubuk, D. K. Campbell, and H. S. Park, Accelerated Search and Design of Stretchable Graphene Kirigami Using Machine Learning, Phys. Rev. Lett. **121**, 255304 (2018).

[40] X. Sun, L. Yue, L. Yu, H. Shao, X. Peng, K. Zhou, F. Demoly, R. Zhao, and H. J. Qi, Machine learning-evolutionary algorithm enabled design for 4D-printed active composite structures, Adv. Funct. Mater. **32**, 2109805 (2022).

[41] J. Dong, C. Hu, J. Holmes, Q.-H. Qin, and Y. Xiao, Structural optimisation of cross-chiral metamaterial structures via genetic algorithm, Compos. Struct. **282**, 115035 (2022).

[42] G. X. Gu, C.-T. Chen, D. J. Richmond, and M. J. Buehler, Bioinspired hierarchical composite design using machine learning: Simulation, additive manufacturing, and experiment, Mater. Horiz. **5**, 939 (2018).

[43] G. X. Gu, L. Dimas, Z. Qin, and M. J. Buehler, Optimization of composite fracture properties: Method, validation, and applications, J. Appl. Mech. **83**, 7 (2016).

[44] S. Wu, C. M. Hamel, Q. Ze, F. Yang, H. J. Qi, and R. Zhao, Evolutionary algorithm-guided voxel-encoding printing of functional hard-magnetic soft active materials, Adv. Intell. Syst. **2**, 2000060 (2020).

[45] J. Zheng, S. Li, and B. Wang, Design of low-frequency broadband flextensional transducers based on combined particle swarm optimization and finite element method, Smart Mater. Struct. **30**, 105002 (2021).

[46] See Supplemental Material at http://link.aps.org/supplemental/10.1103/PhysRevApplied.18.054050, which includes supporting videos, analytical explorations, details of the FE simulations, and descriptions of the experiments.

[47] D. Wang, Y. Xiong, B. Zhang, Y.-F. Zhang, D. Rosen, and Q. Ge, Design framework for mechanically tunable soft biomaterial composites enhanced by modified horseshoe lattice structures, Soft Matter **16**, 1473 (2020).

[48] I. F. Ituarte, N. Boddeti, V. Hassani, M. L. Dunn, and D. W. Rosen, Design and additive manufacture of functionally graded structures based on digital materials, Addit. Manuf. **30**, 100839 (2019).

[49] M. Mirzaali, A. H. De La Nava, D. Gunashekar, M. Nouri-Goushki, R. Veeger, Q. Grossman, L. Angeloni, M. Ghatkesar, L. Fratila-Apachitei, and D. Ruffoni, Mechanics of bioinspired functionally graded soft-hard composites made by multi-material 3D printing, Compos. Struct. **237**, 111867 (2020).

[50] F. Liu, T. Li, X. Jiang, Z. Jia, Z. Xu, and L. Wang, The effect of material mixing on interfacial stiffness and strength of multi-material additive manufacturing, Addit. Manuf. **36**, 101502 (2020).

[51] J. Liu and Y. Zhang, Soft network materials with isotropic negative Poisson's ratios over large strains, Soft Matter **14**, 693 (2018).

[52] G. C. Engelmayr, M. Cheng, C. J. Bettinger, J. T. Borenstein, R. Langer, and L. E. Freed, Accordion-like honeycombs for tissue engineering of cardiac anisotropy, Nat. Mater. **7**, 1003 (2008).

[53] M. Vatankhah-Varnosfaderani, W. F. Daniel, M. H. Everhart, A. A. Pandya, H. Liang, K. Matyjaszewski, A. V. Dobrynin, and S. S. Sheiko, Mimicking biological stress–strain behaviour with synthetic elastomers, Nature **549**, 497 (2017).

[54] A. Pissarenko and M. A. Meyers, The materials science of skin: Analysis, characterization, and modeling, Prog. Mater. Sci. **110**, 100634 (2020).